Automated detection and Characterization of wave structures obtained from GNSS measurements.

Olusegun Jonah, Pablo Reyes, Leslie Lamarche, Anthony van Eyken*
SRI International Geospace Group, Menlo Park, California.

A simple technique designed to automatically identify and characterize wave structures from Total Electron Content (TEC) data obtained from Global Navigation Satellite System (GNSS) satellites and multiple receiver stations is presented. We used 11 years of GNSS data (one complete solar cycle) to detect and characterize the traveling ionospheric disturbances (or wave structures) over high latitude (65ºN + 5º, 147oW + 5º – Poker Flat, AK) and middle latitude (40ºN + 5º, 117ºW + 5º - Mt. Moses, NV) regions. The algorithm is capable of automatically detecting basic wave parameters such as wave period, horizontal phase velocity, amplitude, wave propagation direction and wavelength. The designed algorithm can be applicable in the following areas: (1) widely applicable to GNSS-TEC data globally (2) easily apply in climatology study of wave analyses. (3) serves as input into innovative machine learning (ML) algorithms ABCGAN (e.g., Valentic 2023 designed to characterize background ionospheric plasma and predict wave-like high/low-frequency perturbations). (4) serves as anomaly detection for real-time scenarios. Furthermore, we apply the developed wave detect and characterization technique to investigate three rockets launched on January 26 and 28, 2015. We examine the distribution of different scales of TIDs, and how they varied from high (Poker Flat) to middle (Mt. Moses) latitudes. Lastly, we show that the wave structures at the high-latitude regions of Poker Flat are substantially affected by auroral processes and those from the middle-latitude regions of Mt. Moses are impacted by AGWs coupling from below.

Keywords: Automated wave detection; GNSS-TEC, LSTIDs, MSTIDs, Wave parameters; differential TEC estimation method, Rocket induced Ionospheric disturbances

Main Points:

(1) The computation approach and characterization of wave parameters using GNSS-TEC data.
(2) Morphological statistical distribution of LSTIDs and MSTIDs from 11 year of GNSS-TEC data over Poker Flat and Mount Moses.
(3) Results also show ionospheric perturbation induced by rocketing lunching.

1.0 Introduction

The upper atmosphere plays host to a variety of complex plasma dynamics owing to the solar radiation, energy transfer, electromagnetic fields, and plasma processes. These complexities are known to generate different kinds of wave perturbations such as atmospheric gravity waves (GWs) and associated traveling ionospheric disturbances (TIDs). TIDs are the indication of GWs in the ionosphere and can be described as plasma density fluctuation that propagates as waves through the ionosphere with a wide range of velocities and frequencies. TIDs play an important role in the exchange of momentum and energy between various regions of the upper atmosphere and are relevant for studying the coupling processes in the thermosphere and ionosphere system (e.g., Hunsucker, 1982; Hocke & Schlegel, 1996 Akeem et al. 2015, Zhang et al. 2019, Komjathy et al. 2016, Meng et al 2019).

TIDs can be classified according to their wave velocity, wavelength, and period. Large Scale TIDs (LSTIDs) have horizontal propagation velocities between 400 m/s and 1000 m/s, horizontal wavelengths greater than 1000 km (1000–3000 km) and periods in the range of 30 min to 3 h. Medium-scale TIDs (MSTIDs) have horizontal propagation velocities between 150 m/s and 1000 m/s, horizontal wavelengths of several hundreds of km and periods between 15 min and 60 min. Although there is some variability in these parameters, these ranges have been reported by many studies (Hocke and Schlegel (1996), Hunsucker (1982) and Zhang et al. (2019)). LSTIDs are mostly driven by auroral and geomagnetic activity (e.g., Figueiredo et al., 2017, Jonah et al. 2018). As such, they can provide some indication of solar wind-magnetosphere-ionosphere coupling. LSTIDs can also be generated within the vicinity of the magnetic equator (Habarulema et al., 2018). MSTIDs on the other hand are mostly associated with ionospheric coupling with the lower atmosphere (Hunsucker, 1982). Experimental observations of transient events during ionosphere–troposphere coupling events such as tsunami (e.g., Savastano et al., 2017); anthropogenic activities (e.g., Jonah et al 2021), and convective storms (e.g., Azeem et al., 2015). MSTID drivers can be used to specify the level of ionosphere–thermosphere-lower atmosphere coupling and the connection between processes on the Earth's surface and the upper atmosphere (Lastovicka, 2006).

For several decades, many authors have shown how TIDs generated by GWs (GWs-TIDs) can be triggered from various sources. Richmond, (1978); Hunsucker, (1982); Zhang et al. (2019) and Jonah et al. (2018 and 2020) show AGWs-TIDs can be generated in auroral regions from Joule heating caused by enhanced geomagnetic storm condition. Vadas et al. (2012) and Azeem et al (2017) show how severe meteorological events such as thunderstorms and tornadoes can generate AGWs-TIDs which can appear as concentric rings at higher altitudes if the intervening neutral winds are small. The signatures of concentric AGWs-TIDs have also been observed in the ionosphere by Nishioka et al., (2013) and Azeem et al., (2015 and 2017). Several authors have shown that deep convection in the troposphere is one of the primary drivers of concentric AGWs-TIDs that can propagate upward into the mesopause and ionospheric regions [Alexander, 1996; Holton and Alexander, 1999; Lane et al., (2001); Vadas and Fritts, 2009; Vadas et al., 2009; Jonah et al. (2016)]. Recent theoretical studies have also shown that some AGWs from deep convection can also propagate efficiently into the thermosphere [Vadas, 2007; Kherani et al., 2009; Vadas and Crowley, 2010; Vadas et al., 2014]. Anthropogenic event or man-made activities; nuclear detonations as well as earthquakes-tsunamis and other transient events (such as rocket lunching, earthquakes and tornado events) are potential sources of smaller scale AGWs-

TIDs in Earth's atmosphere [Hines, 1967; Artru et al., 2005; Liu et al., 2006; Lognonńe et al., 2006; Rolland et al., 2010; Komjathy et al., 2016; Jonah et al., 2021]. Furthermore, the investigation of AGWs-TIDs using dense GNSS receiver network, which can be used measure the TEC along satellite-receiver paths with high temporal resolution, has been proven to be a practicable means of observing and studying different kinds of wave structures and their associated irregularities in the upper atmosphere [Zhang et al. 2017, Coster et al. 2017; Komjathy et al. 2016; Jonah et al. 2018, 2021]. Giving the densely distributed GNSS-receivers and easy access of the measurement globally, GNSS observations have been widely used to study the spatial variations and other characteristics of traveling ionospheric disturbances (TIDs) and other wave structures. However, most studies determine wave properties by manually examining a series of keogram/hodogram figures or by inspecting time varying density/TEC maps. This approach is not only prone to human errors but also liable to information overload and mental bias and is often subject to ambiguity or decision fatigue. As a result, we have seen evidence of discrepancies in observational results and consequent interpretations of TIDs or wave structure analysis in the literature. For example, the climatology study by Kotake et al. (2006) over southern California showed daytime MSTIDs with the velocity, period, and wavelength of 80–180 m/s, 20–35 min, 100–250 km respectively. Whereas the study by Ding et al. (2011) over central China reported daytime MSTIDs with velocity and period of 100 – 400 m/s, 20–60 min. On the other hand, the study by Figueredo et al. (2018) over South America reported daytime MSTIDs with velocity, period and wavelength of 323 ± 81 m/s 24 ± 5 min, 452 ± 107 km, respectively. While the case study of daytime MSTIDs over similar locations in South America by Jonah et al. (2016) shows that MSTIDs are characterized with 255-389 km wavelength, 122 – 189 m/s, and 20 – 55min periodicity. These discrepancies in the wave parameters do not only result from different sources or locations of the waves but could also be due to the approaches used in identifying and classifying the wave parameters by the many authors. Furthermore, Belehaki et al., (2020) worked on Warning and Mitigation Technologies for Traveling Ionospheric Disturbances (Tech-TIDE), where they exactly identified and tracked TIDs with different scales. Recent paper by Borries et al (2023) also worked on a new TID index (ATID), which is based on correlation analysis with upper atmospheric drivers and approach for LSTID detection. These studies dealt with identification and prediction of wave but not classifications of their parameters. The present study focuses on the determination and classification of wave parameters which is important for wave source identification and characterization. In this study, we describe the simple approach of automatically detecting wave parameters, including the direction of propagation, wavelength, velocity, and period of the wave. We also present some case studies of small scale TIDs from transient events (rocket launching events). Lastly, we present the climatology and statistics analysis of MSTIDs and LSTIDs from 11-year data computation. The climatology and statistics studies as well as different analysis of various driving sources will be detailed in future work.

2.0 Methodology: Automated wave detection

2.1 Method of processing GNSS-TEC from multiple RINEX observations

The technique for processing TEC from multiple dual-frequency global navigation satellite system (GNSS) receivers have been developed by numerous authors (e.g. Mannucci et al, 1998; Komjathy, 2005; and Coster and Rideout, 2006). The MIT Automated Processing of GPS (MAPGPS) developed by Coster and Rideout (2006) is employed for the current study because of the efficient method of calculating the receiver biases. The method of calculating the individual receiver biases is essential for accurate TEC estimation because one of the largest sources of error in estimating TEC from GPS data is the determination of the unknown receiver biases. Thus, the bias determination procedure for the MAPGPS has recently been updated by using newly developed weighted linear least squares of independent differences (WLLSID) as described in Vierimen et al. (2016). TEC results from MAPGPS algorithm have been validated/used by many researchers in numerous publications (e.g. Jonah et.al 2018, 2020, Zhang et.al 2019; Coster et. al. 2017 etc). There are several steps involve in the automated processing of MAPGPS TEC:

(i) download and read all versions of RINEX, and other data formats. The RINEX files consist of the observables such as the L1 and L2 frequencies as well as the satellite position which are used to estimate the TEC (Mannucci et al, 1998).

(ii) The ionospheric delay ($\Delta\rho$) on GPS signals can be described in terms of TEC, inversely proportional to a square of frequency. :

$$\Delta\rho = \frac{40.3}{f^2} TEC$$

(iii) Calculate STEC by integrating electron density along the signal path from each receiver to all satellites using a combination of processed f1 and f2 frequencies on L1 and L2 pseudorange and phase data. Screen for and correct Loss of lock in the carrier-phase observables (Blewitt 1990), and use the carrier-phase to smooth the pseudorange values:

$$STEC = \frac{f_1^2 f_2^2}{40.3(f_1^2 - f_2^2)} (\phi_2 - \phi_1)$$

where f_1 and f_2 are the GPS L1 and L2 frequencies, Φ is the carrier phase measurement,

(iv) compute the receiver and satellite biases, *b*, *c* respectively. The step-by-step method of calculating instrument bias are explained in Vierimen et al. (2016). Biases represent the additional delay between measured L1 and L2 GPS signals at the receiver due to both satellite and receiver hardware. The TEC with instrument bias considered is call the absolute TEC and is given as:

$$ATEC = b + c + \mathrm{STEC} + \Im$$

where, b is the receiver bias, c is the satellite bias, and $\Im$ is the measurement noise. The measurement is scaled to total electron content (TEC) units, i.e., $10^{16}\mathrm{m}^{-2}$. (Coster and Rideout 2006; Vierimen et al. 2016)

(v) compute the mapping function, which is the multiplicative factor used to convert line of sight TEC to vertical TEC. The TEC obtained here is referred to as vertical TEC (VTEC). The mapping function used is given as:

$$z = \frac{1}{\sqrt{(1.0 - (Fcos(el))^2)}}$$

where $F = (1 + \left(\frac{h}{R_E}\right))^{-1}$ and *h = 335 km* and *RE is the radius of the earth given as* 6378.1 km.

Lastly, a 30-degree cutoff elevation for ground-satellite ray paths is used to eliminate data close to the horizon. For the further description of the above TEC estimation processing see Coster and Rideout et al. (2006) and Vierimen et al. (2016).

2.2 Differential-TEC estimation method

After obtaining the STEC and VTEC in the processes explained in section 2.1, we developed an algorithm to compute the differential-TEC (diff-TEC) and an automated procedure to detect and identify seven different wave structure parameters. In the analysis discussed below, we first described the estimated method of obtaining the diff-TEC, followed by the wave parameter detection procedure.

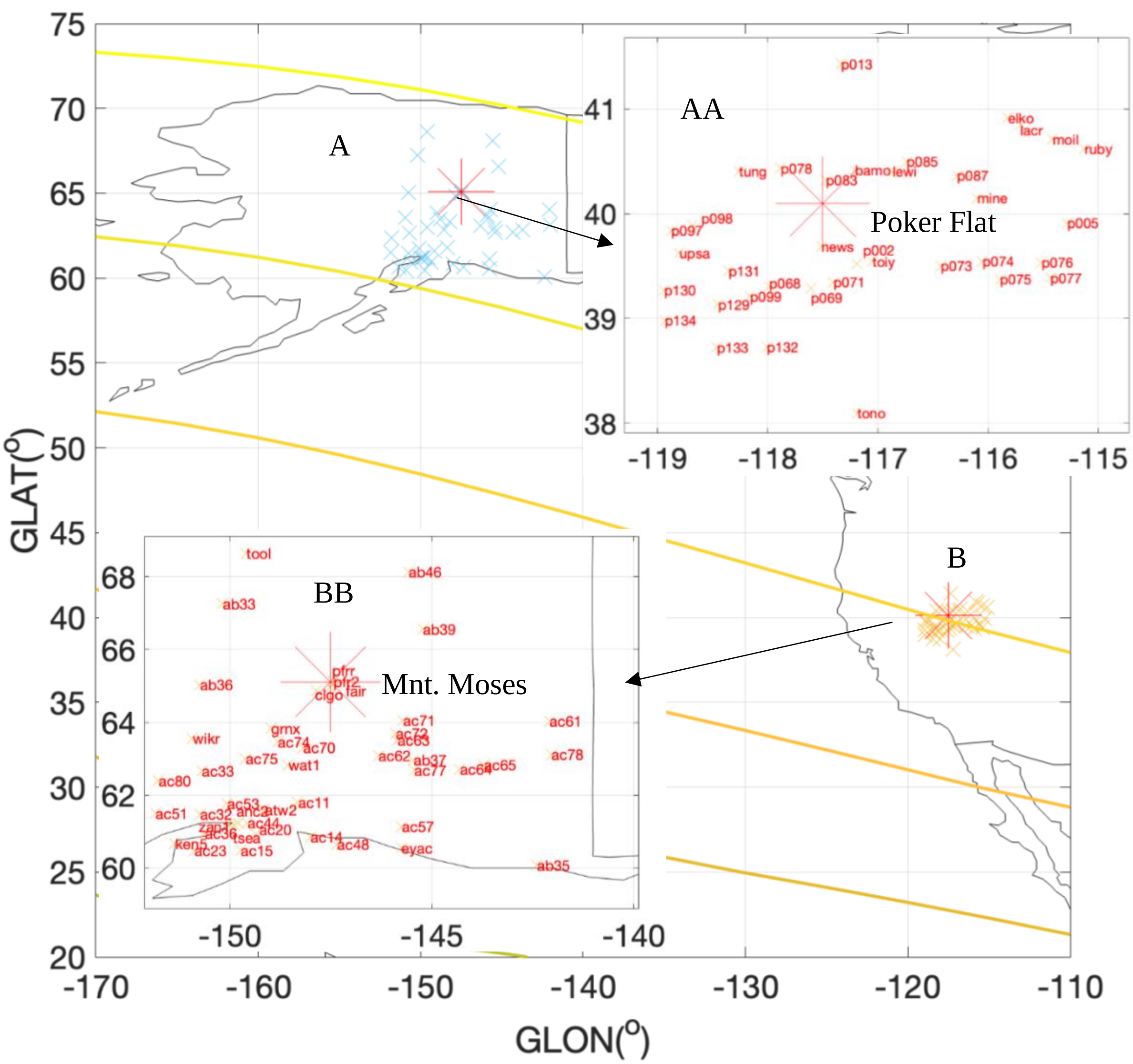

Figure 1. A and B represent examples of the GNSS receiver station distribution within ±5 degrees (for 2015, Jan 28) over Poker Flat and Mount Moses respectively. AA and BB represent the zoomed images and station names of A and B. The colored horizontal lines represent magnetic field lines over North America.

In this study, we focused on GNSS TEC data around Poker Flat (within +5 degrees) to extract different wave structures. More than 40 GNSS receiver stations found within the radar perimeter (65°N ± 5° latitude, 147°W ± 5° longitudes) are used in our analysis (see Figure 1). Each receiver station is used to collect measurements from all satellites in view and are passed through our designed wave processing procedure discussed below. First, determine the kind of filtering software best suited for our analysis. There are three main types of filtering applications that are commonly used by researchers. (a) the polynomial filtering method (; Jonah et al. 2016); (b) the low-pass Savitzky-Golay filter (e.g. Savitzky & Golay, 1964; Zhang et al. 2019) and band-pass filter approach (e.g. Jonah et al. 2020). We disregard the polynomial filter as It is well known that it becomes unstable with high degrees. After examining the two other most used method that is, the bandpass and the Savitzky & Golay low pass filter (refer to the supporting material), we found the bandpass method most suitable for this application.

2.3 Procedures for wave identifications

There are three main stages: (stage 1) the computation of TEC: This can be obtained from Madrigal website or processed using alternative methods as discussed above. Stage 2 involves the computation of wave structure according to the following steps: First, it is important to note that 3 days (centered around the day of interest) are need for the wave parameter computation. This helps to limit/eliminate edge effect problem which usual occur in filtering analysis. Figure 2 illustrates the flow-chart of the approach and measures taken to ensure cleaned input data before the zero-phase Butterworth bandpass filtering analysis is applied. These procedures are explained as follows: (i) Five hours of data centered around the period of interest which make approximately one satellite arc period is collected and arranged in a time sequence. (ii) All multiple NaN values (i.e., large data gaps) as a result of data arrangement in time are removed and dataset with one or two NaN values are interpolated using nearest neighbor interpolation method. (iii) Remove data where NaNs cover over half the 5-hour window (iv) All forms of discontinuity e.g., data gaps due to cycle slips, multipaths, or power outages are detected and removed from the analysis. (v) Next the data is detrended to remove any trend in the dataset that can make the filter bias towards normal day-to-day variation of the data (vi) The edge effects are avoided by repeating 10% of the dataset to both ends of the original data before applying the filter. This is known as padding technique. (vii) The bandpass filter analysis is then carried out and the 10% padding data are removed from the boundaries before we continue with the rest of the process. (viii) After the filter analysis is done, the following measures are taken to avoid misinterpreting noise as signal or wave structures. (a) we reject wave amplitudes that are less than 10% of the TEC amplitude. (b) we reject signal to noise ratio (S/N) that are not up to 1.1 or 0.04 TECU. (c) for medium scale waves, we reject periods less than 5 min, which is the Brunt Vaisala peak period for wave propagations (Snively and Pasko, 2003).

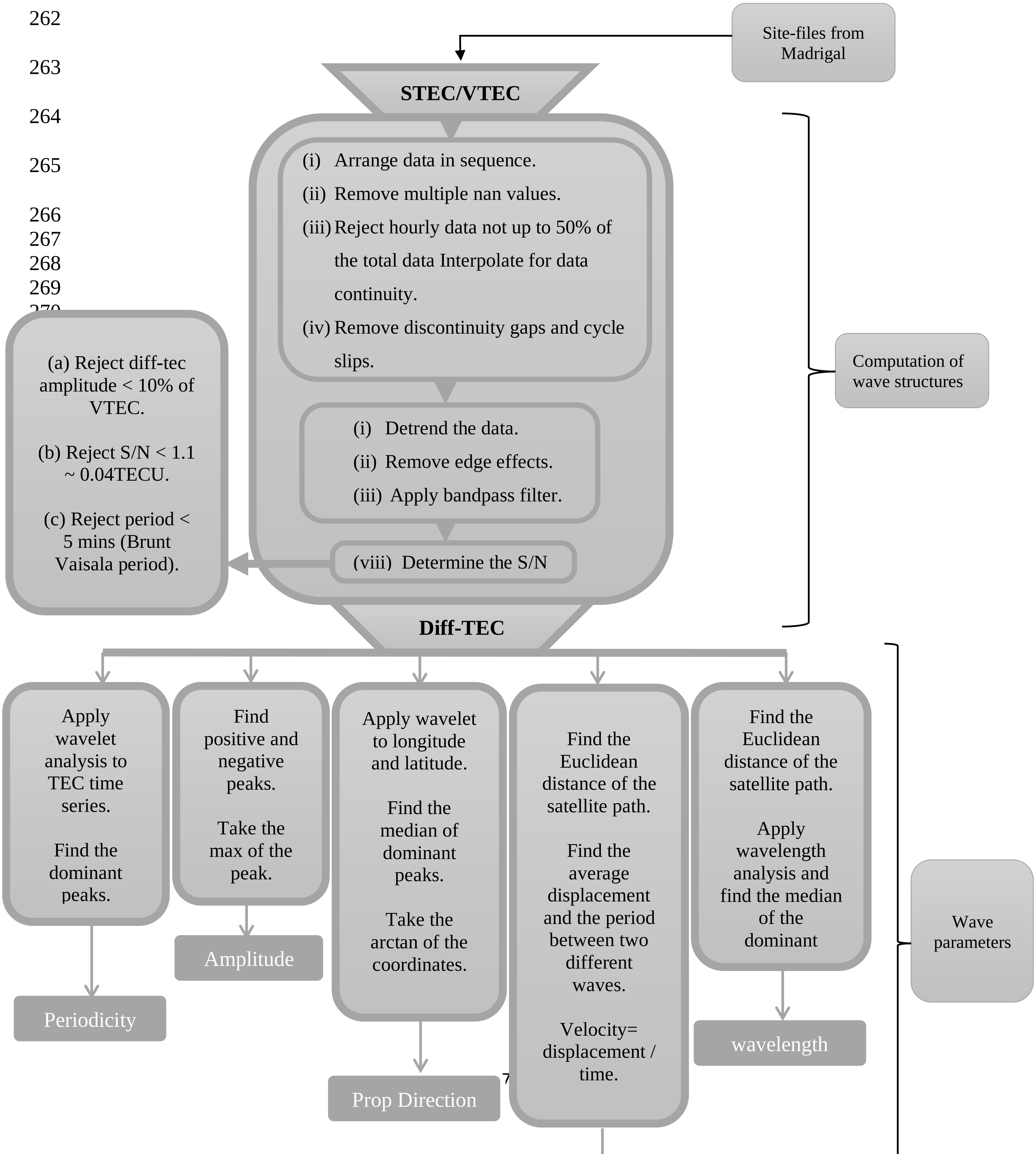

Figure 2. flow chat illustrating different processing stages of the wave detection algorithm.

Figure 3 illustrates examples of how edge effects and artifacts can occur if gaps and discontinuities in the data are not handled carefully following the above procedure. Figure 3(a) shows the data gap observed from the interaction between ac53 receiver with prn 31. Figure 3(b) demonstrate the result when measures are not taken, the filter artificially create a strong wave (above noise level) that can be mistaken for proper wave structure. Furthermore, Figure 3(c), shows that the bandpass filter works well both at when smaller window data are used to avoid data gap and when large window (without data gap) is used. The blue and cyan curves illustrate the application of whole data and 15 min window dataset. Lastly, in Figure 3(d), we show an example of when edge effects are or is not considered. The blue and green curves show the results with and without considering the edge problem. The blue curve at the onset of wave could easily be mistaken for higher amplitude. This is just filtering error as a result of edge problems.

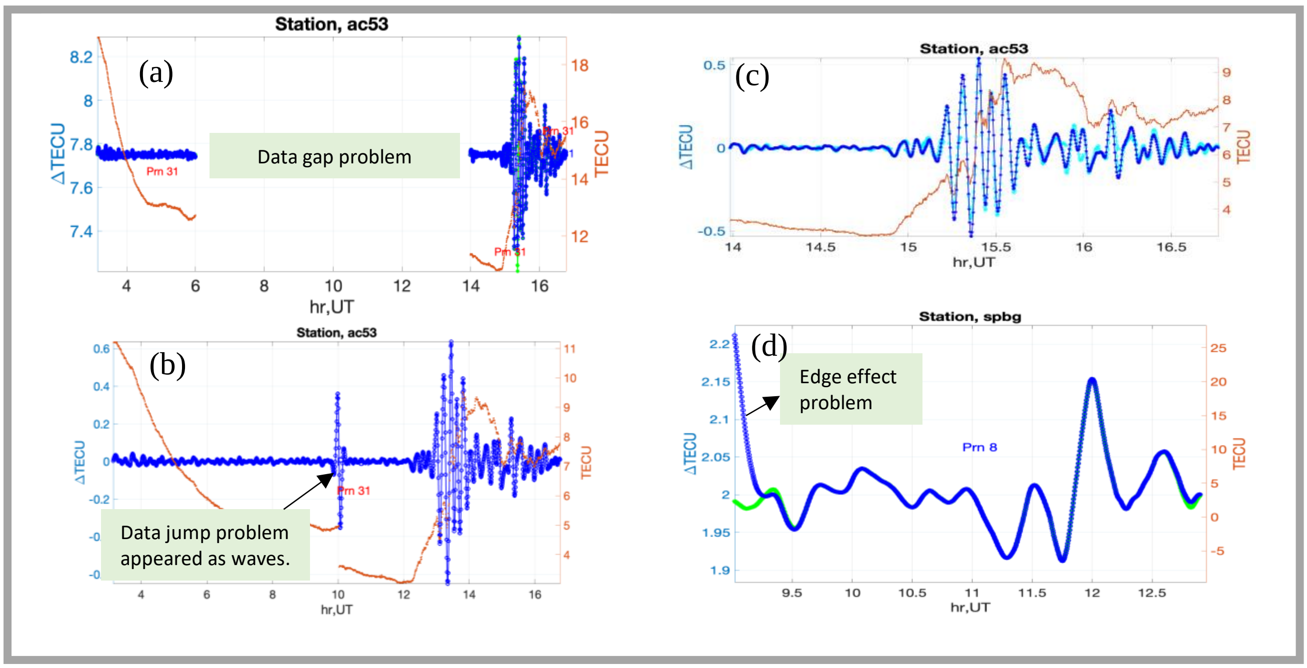

Figure 3. (a) shows wave structures (diff-TEC) obtained from a zero-phase Butterworth bandpass filter considering the data gaps, (b) shows diff-TEC obtained from bandpass filter without considering the data gaps. Blue and red curves represent the diff-TEC and TEC respectively. (c) Blue color shows diff-TEC. The cyan color is derived from bandpass filter with a 15-minute window interval. (d) Blue color shows the wave analysis without edge effect treatments. Green color shows wave analysis with edge effect treatments.

2.4 Estimation of different wave parameters

The third stage (stage 3) describes how our algorithm compute wave parameters (periodicity, horizontal wavelength, wave propagation direction, and wave velocity) as observed the satellite receiver pair from GNSS-TEC data. Detail discussion is given below. At least two receiver stations and all available satellite-receiver paired are need. Two receiver stations are particularly needed to calculate the wave velocity and all the prn (satellite) are average out to compensate for the satellite motion's effect on the estimated wave velocity. More detail explanations about this procedure will be discussed later in this section.

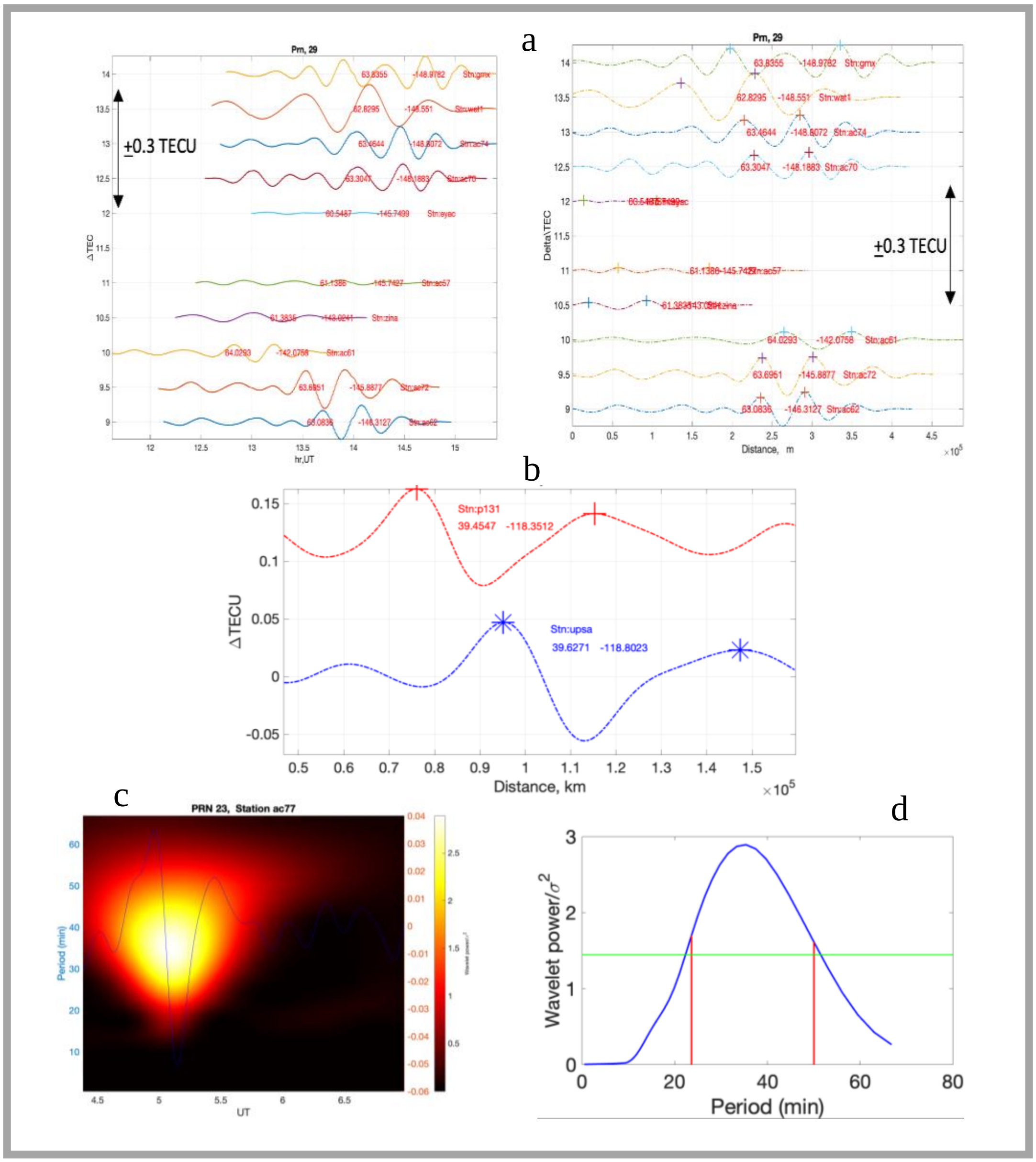

Figure 4(a) Wave structures from multiple receiver stations. Left panel shows diff-TEC as a function of time to obtain the period. Right panel shows similar wave structure but plotted as a function of distance to obtain the wavelength. Figure 4(b) The red and blue curves represent wave structures from single PRN, but two different receiver stations used for the computation of phase velocity. Figure 4(c) Wavelet analysis showing example of dominant periodicity. Figure 4(d) represents the tracing-out of the dominant period of the wavelet analysis, the vertical red lines and the horizontal green line are used to trace-out the dominant period.

(i) Period: The wave period is obtained by taking the spectra analysis of estimated wave structure as a function of time using Morlet wavelet transform. The peak amplitude of the wavelet transform is the period (Figure 4(c and d)).

(ii) Wavelength (λ): To calculate the λ, we first calculate the Euclidean distance using the latitude *(lat) and* longitude *(lon)* information from the satellite PRNs. Euclidean distance (EU_D) is calculated from the ECEF coordinates of the PRN location relative to the ECEF coordinates reference point using the Pythagorean theorem.

Note: reference point is the epicenter coordinates of the particular event of interest. The wavelength is finally determined by taking the spectra analysis of wave structure as a function of estimated Euclidean distance using Morlet wavelet transform.

(iii) Velocity (vel): To calculate the velocity, two adjacent stations are required, and two different approaches were used.

a. From Figure 4(b), the algorithm finds two dominant consecutive peaks (point A and point B) from the two wave structures obtained from each satellite-receiver-pair, measures the distance between point A and B (red curve) and point C and D (blue curve) which are the two dominant peaks and take their average. The average time difference associated to these points are also noted. Lastly, the change in displacement (ΔX), and change in time (ΔT), are used to compute the wavelength (λ), period (τ) and consequently, the velocity (λ / τ) of the waves. This process is implemented for all specific receiver stations and all PRNs in view, then average-out to minimize the error from satellite motion.

b. The relationship between frequency *(f)*, and wavelength *(λ)* of wave property (i.e., $f \lambda$), where $f = 1/\tau$ is applied to estimate the wave speed. A continuous wavelet transform was performed and applied to analyze the wave structure as a function of time and Eu_D (see Figure xx5(c)). This technique allowed us to identify the dominant periods and dominant wavelengths in a particular wave structure (as shown in Figure 4(d). Then, the λ / τ relation is applied to estimate the speed of the observed waves. The percentage difference between the 'first approach' and the 'second approach' for measuring wave speed is calculated to be ~0.56%, which indicate good consistency in both approaches.

(iv) Wave Propagation direction (∅): To determine the orientation of wave propagation (with bearing angle from north), we applied the Morlet wavelet transfer to the wave oscillation in the latitudinal and longitudinal directions. This allows us to estimate wavelength in both in the latitudinal and longitudinal directions (Haralambous and

Paul, 2023; Hocking, W.K. 2001). Assuming the meridional wavelength is related to the wave observed in the latitudinal wavelength which is given by $2\pi/k\hat{y}$ and the horizontal wavelength is related to the wave observed in the longitudinal wavelength given by $2\pi/k\hat{x}$. Thus, the direction of wave propagation direction can be defined as

$$tan\emptyset = \frac{\lambda_x}{\lambda_y} = \frac{2\pi}{k_x} * \frac{k_y}{2\pi} = \frac{k_y}{k_x}$$

where k_y and k_x are waves in the longitudinal and latitudinal directions respectively.

The four-quadrant inverse tangent is used to resolve the phase ambiguity of atan $(\frac{\lambda_x}{\lambda_y})$. Furthermore, given that wavelet function output cannot be negative values, we obtained the negative sign of the waves (i.e. westward or southward directions of the waves) by identifying the dominant wavelength that falls on the southern and western side of the reference station from the wave oscillation and apply the sign to the λ_x $(latitude)$ or λ_y $(longitude)$.

3.0 Results and Discussions

3.1 Specific Case studies

The frequency of rocket lunches has increase over the years. Recently, SpaceX successfully launched its massive Falcon Heavy rocket for the first time on 6 February 2018. This signals a new era of space exploration and facilitate the study of space and atmospheric science. Many researchers have shown that rocket launch events are potential sources of ionospheric disturbances around the lunch sites (Afraimovich et al., 2002; Bowling et al., 2013; Lin, et al., 2017a). The blast impact generated as a consequence of these launch events can cause strong sharp changes in pressure, temperature, density and electrical conductivity (Drobzheva et al. 2003). According to Mendillo, (1981) the dominant cause of atmospheric perturbations due to rocket exhaust is mainly associated with the variety of chemical reactions that can occur between molecular materials and the neutral and ionized components of the atmosphere. Lin, et al. (2017b) first reported the rocket induced shock waves and concentric TIDs (CTIDs) using Global Positioning System TEC over California-Pacific region. They suggested that the CTIDs are the manifestation of concentric gravity waves that were originated from the mesopause region. Here we use the ground-based Global Navigation Satellite System (GNSS) network over Poker Flat to observe the ionospheric responses to three different rocket launch. The GNSS's wide coverage with dense TEC observations provides an opportunity to monitor the onset and evolution of rocket-induced atmospheric waves. In this study, we investigate the consequent effect of the rocket launch by using GNSS-TEC dataset to examine the atmospheric changes resulting from these transient events during and after the launches. We analyzed three different rocket launch events from the Poker Flat Rocket Range in Alaska: the NASA 46.009 UE, NASA 46.010 UE both launched on January 26 with apogee of 160 km, and the NASA 49.002 UE launched on January 28 with an apogee of 590km. Detailed information about these events are indicated in the Table 1.0. We observed wave propagation in the direction of the lunch, relatively small amplitude, short-period ionospheric and velocity in the range of sound waves. The wave characteristics of rocket event that reached 160km is similar with that of the rocket event that reached 590km as shown in Figure 6 and 7.

Table 1.0. Information about rocket launches over Poker Flat on 26 and 28 of January 2015

Vehicle Number	Launch Date (GMT)	Launch Hours (GMT)	Nominal Apogee Altitude (km)	Perturbed time delay
NASA 46.009UE	1/26/15	09:13	160 km	16min
NASA 46.010UE	1/26/15	09:46	160 km	14min
NASA 49.002UE	1/28/15	10:41	590 km	06min

Powerful rocket launching has been demonstrated to cause disturbances in the upper atmosphere (Mendillo, 1981; Afraimovich et al, 2002). Mendillo, (1981) observed ionospheric hole phenomenon which was considered to result from the following three coupled processes: (1) diffusion of an exhaust cloud of highly reactive neutral molecules through a tenuous, multi-constituent atmosphere, (2) chemical reactions between the expanding cloud and the various species (ions and neutral) in the atmosphere, and (3) solar and/or dynamical replenishment processes. While Afraimovich et al (2002) recorded Shock Acoustic Wave (SAW) with azimuth angle of the wave vector that varies from 30° to 60°, and the SAW phase velocity of 900 – 1200 m/s coordinated with the sound velocity at heights of the ionospheric *F*-region peak. Review paper by Karlov et al. (1980), shows that the oscillation period of the ionospheric response, obtained from the Apollo rocket launching mission, varied from 6 to 90 minutes , and the propagation velocity was in the range from 600 to 1670 m/s.

Figure 5. indicate that there was a minor geomagnetic storm on January 26, 2015, around the time of the NASA 46.009UE and NASA 46.009UE rocket launches. To eliminate the influence of the geomagnetic condition during the launch period, we use the bandpass filter with a period of 5 to 15 min (Chou et al. 2018). This allows us to extract only wave perturbations generated by the launch activities. Previous studies have shown that the periodicity of wave structures induced by rocket launch, or other anthropogenic or transient events ranges between 6 - 8 min and the waves structures generated from geomagnetical activities are usually above 60 min periodicity (Richmond, 1978; Hunsucker, 1982; Zhang et al. 2019 and Jonah et al. 2018 and 2020). Therefore, by using the above filter band width have eliminated the effect of geomagnetic storm on our data.

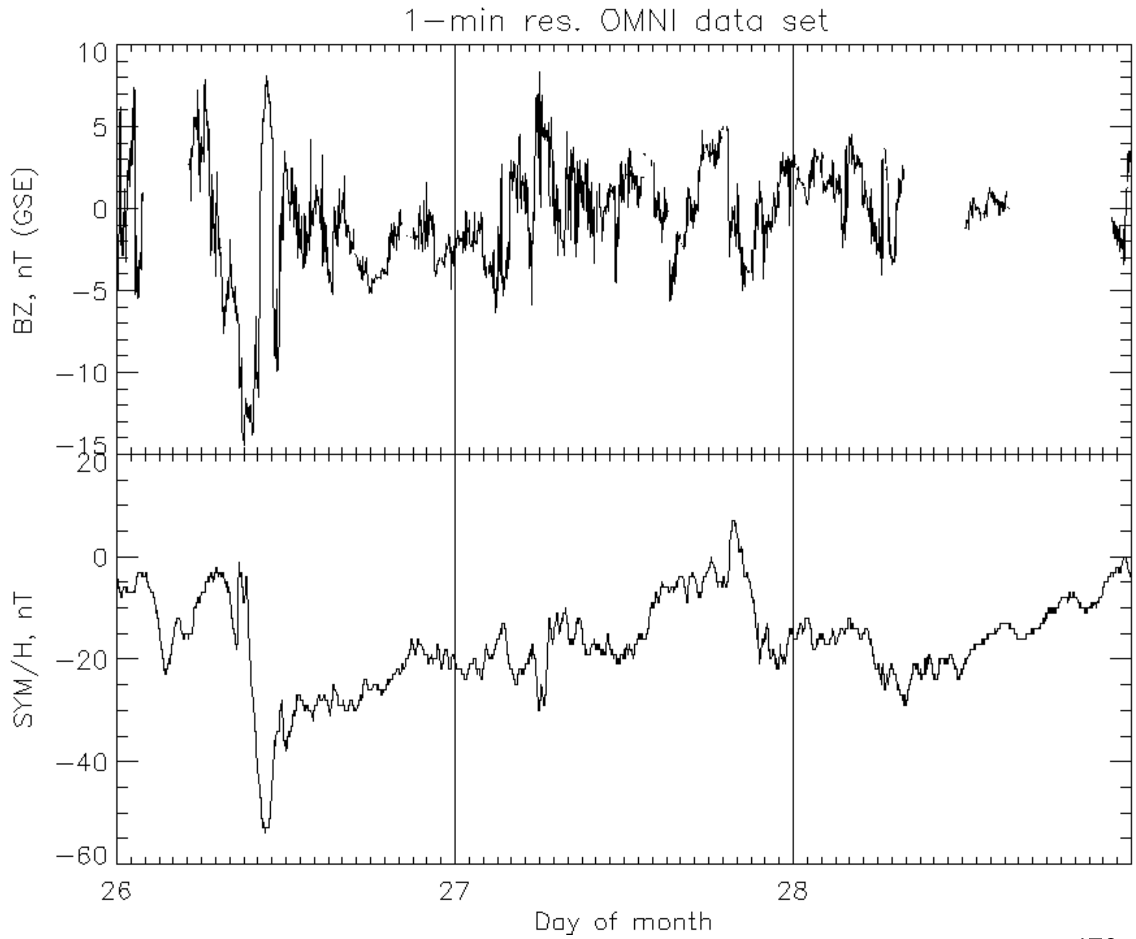

Figure 5. Top and bottom panels represent the Bz index and SymH for days 26 – 28 of January. Day 26 show a minor geomagnetic storm activity while day 28 is relatively calm.

Figure 6 (a – d) represents hourly spatial- temporal variation of differential TEC (DTEC) variations for two rocket launch events on January 26, 2015. A strong disturbance can be clearly observed around the launch hour (panel a) at 9:13 UT. It is still possible to observe similar perturbations around same location (at panel b) which could be from the second rocket launch at 9:46 UT. Figure 7(e) represents the hodogram with latitude as a function of time. The red and blue vertical dash line indicate the time of first and second rocket launches. The wave perturbations started appearing after 16 UT and 14 UT of the launch the first and second launch respectively. Panel (f) shows that the wave traveled in the southeastward direction with average velocity of ~600 m/s.

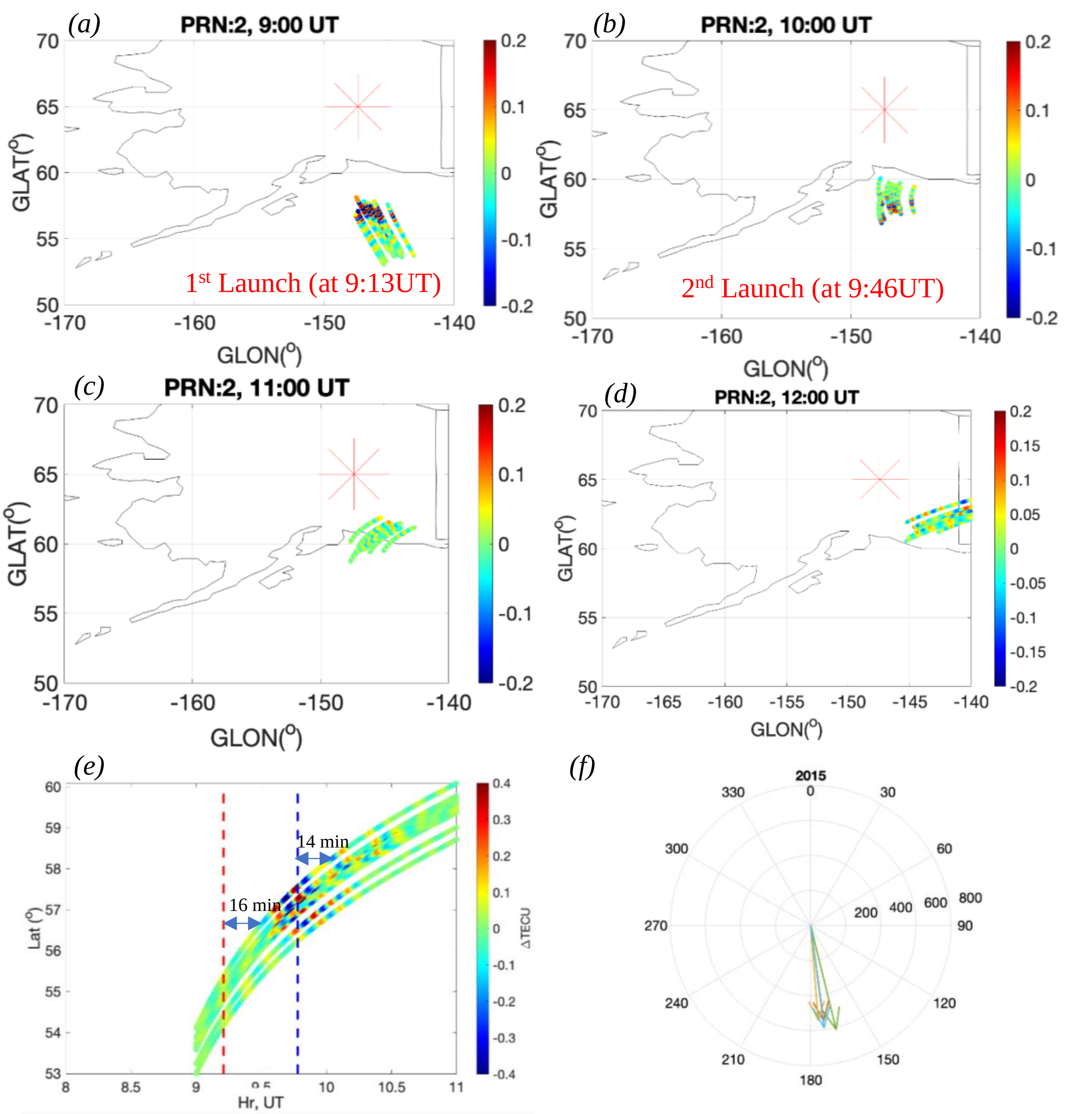

Figure 6 (a-b). represents hourly temporal-spatial variation of differential TEC (DTEC) variations. The star marker represents the location of the launch. Panels e and f represent the hodogram (time/distance diagram) and the polar plot that indicates the direction of wave propagation.

Figure 7 (a – d) also represents hourly temporal-spatial variation of differential TEC (DTEC) variations but for NASA 41.002 UE rocket launch event on January 28, 2015. A strong disturbance can be clearly observed around the launch hour (panel b). Figure 8(e) represents the hodogram with latitude as a function of time. The dash vertical red line indicates the specific time of the rocket launch. It is possible to see that after about 6 – 8 min of the launch the wave structures started appearing close to the to the location of the launch. Panel (f) shows that the wave traveled in the southeastward direction with average velocity of ~600 m/s.

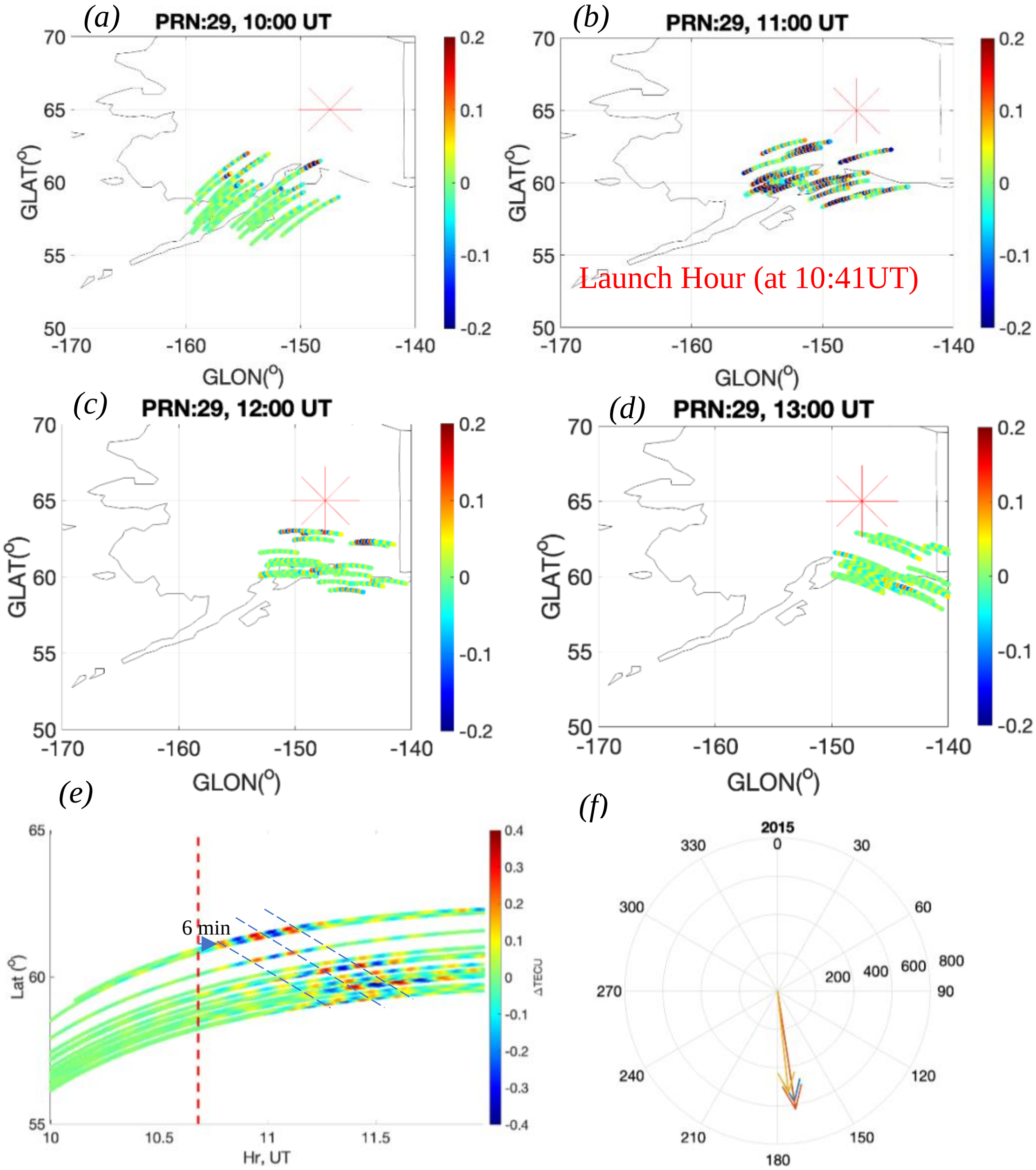

Figure 7 same as Figure YY but for day 28 January 2015.

The wave properties such as velocity, amplitude and propagation direction on Jan 26th events are very analogous with the Jan 28th event except for the time delay. The difference time delay could be as a result of different lunch apogees. The rocket lunches on Jan 26th events only reached 160 km altitude while that of Jan 28th lunch event reach 590km altitude.

3.2 11 Years Wave Distribution Parameters over high and low latitude regions

The processing of GNSS-TEC data to extract and analyze multiple wave parameters are carried out for two locations as shown in Figure 1. One at high latitude (around the auroral region, 65°+5° latitudes) and the other at middle (around 40°+5° latitudes). About 50 GNSS receivers were identified around each region and their RINEX data were downloaded processed.

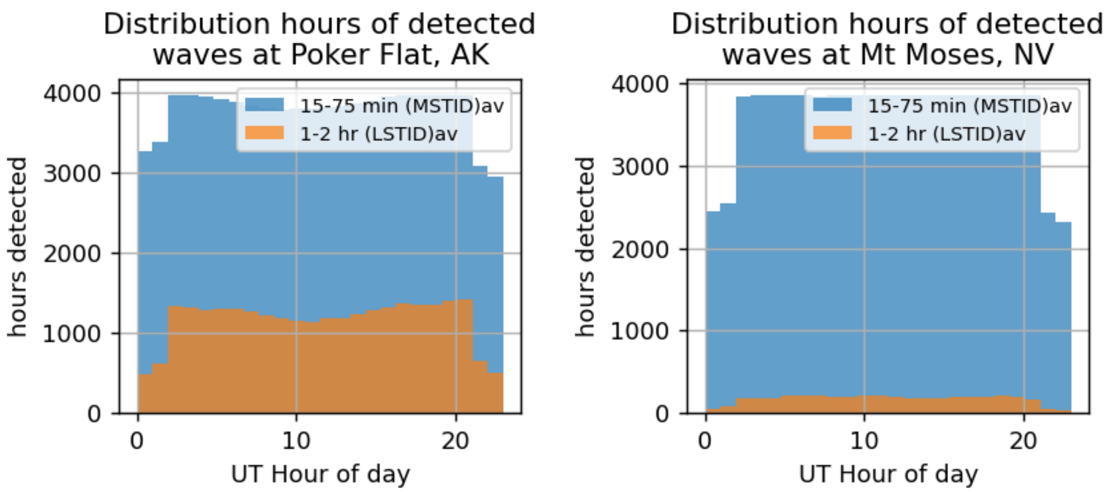

Figure 8 (a) and (b) Distribution of hours detected waves as a function of UT hour of the day for Poker Flat, AK and Mt. Moses, NV respectively.

Figure 8 (a) and (b)shows distribution of hourly detected waves over high latitude (Poker Flat region) and low latitude (Mt. Moses region) for MSTID and LSTID bands. We found similar wave distribution of MSTIDs (blue color) for both Poker Flat and Mt Moses, but differences in the LSTID distributions at the two sites. An average of approximately 1000 hourly LSTIDs are obtained over 11 years at Poker Flat (which means average of 65 LSTIDs are seen per day), while less 100 hourly LSTIDs are obtained over 11 years period at Mt. Moses (which is equivalent to average of 6.5 LSTIDs per day). Many experimental, model and statistical studies show that occurrence rate of LSTIDs increases with increasing magnitude of kp, ap and AE and local auroral electrojet indices (e.g., Tsugawa et al. 2004; Ding et al. 2007). Fuller-Rowell et al. (1996) used modeling analysis to explain that the energy input in the auroral region can heat the thermosphere, drive equatorward wind surges, which can greatly contribute to the seeding of equatorward-traveling LSTIDs. Similarly, Horvath and Lovell (2010) showed that energy input from the auroral region can heat the thermosphere and propel an equatorward wind, providing a driving force for LSTIDs. Ding et al. (2007) used GPS-TEC data to detect LSTIDs linked to the westward auroral electrojet as detected through decreases in the H and X components of the magnetic field. Jonah et al., (2018), revealed that the observed growth in the LSTID was interconnected with this intermittent energy input from the auroral source into the ionospheric system in a clear indication of magnetosphere-ionosphere coupling. Thus, LSTIDs are commonly generated during geomagnetic storms from the period auroral energy input (Tsugawa, et al. 2003; Jonah et al, 2020) and large subauroral polarization stream-induced ionospheric flows (Zakharenkova et al. 2016; Zhang et al., 2019). Therefore, the high occurrence of LSTIDs over Poker Flat (high latitudes) region is mostly as a result of auroral activity prominent to the region. On the other hand, Mt. Moses, a middle latitude location, mountain waves are very prominent because of the land mountains and valleys topography associated to the region. This mountain wave waves are known to generate gravity waves that can consistently seed MSTIDs (Heale et al., 2016; McLandress et al., 2012).

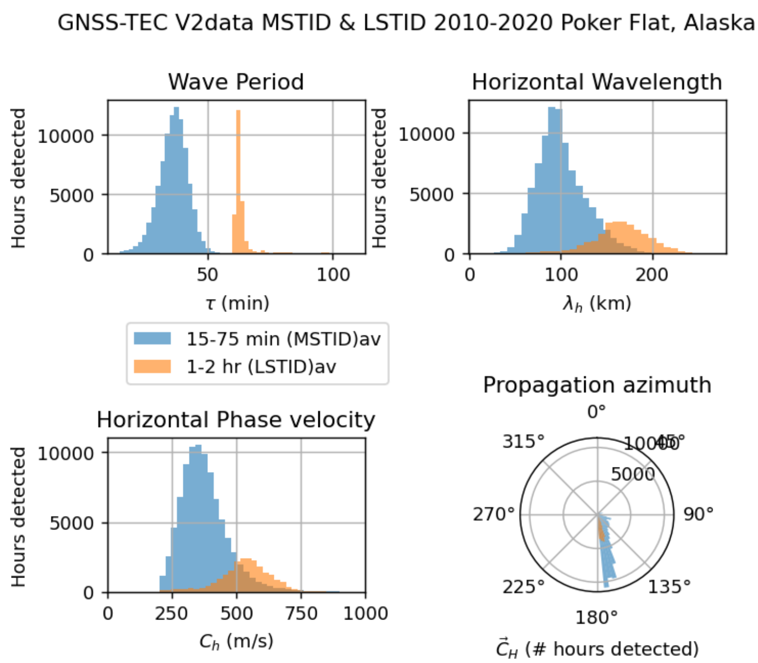

Figure 9 (a-d) represent wave period, horizontal wavelength, horizontal phase velocity and wave propagation direction respectively for High latitude (Poker Flat) region. The blue and brown color represent MSTID and LSTID respectively.

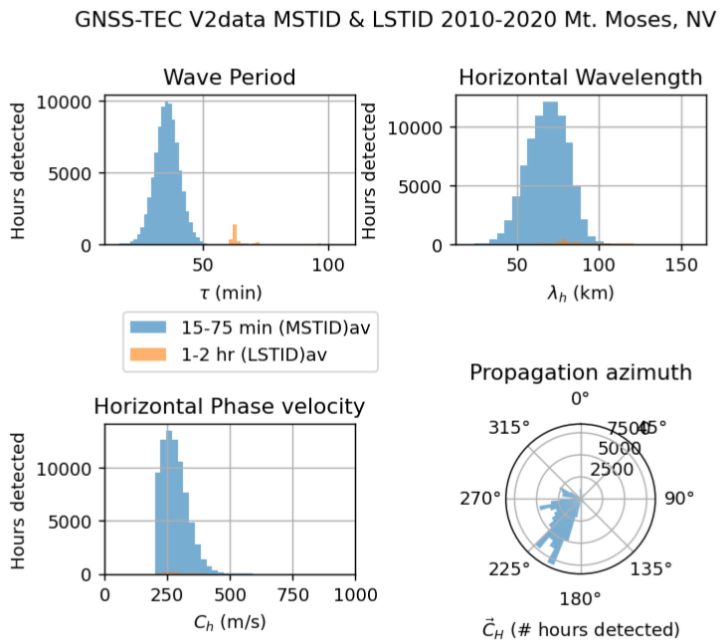

Figure 10 (a-d) same as Figure 9 (a-d) but for middle latitude (Mt. Moses) region.

Figures 9 (a-d) and Figure 10 (a-d) show the summaries of distributions of different parameters extracted around high latitude Poker Flat, AK, and middle latitude Mt. Moses, NV. The period, wavelength and velocity have a more gaussian distribution shape for MSTIDs than for LSTIDs. This is because MSTIDs can be generated very often by regular sources such as weather convection from lower atmosphere (Azeem et al. 2015, 2017; Jonah et al. 2016 and 2018) and other localized sources (e.g., mountain waves). However, the LSTIDs wave parameters (such as velocity and wavelength) for Poker Flat are right shewed, while the LSTIDs wavelength distribution for Mt. Moses is characterized with double gaussian distribution compared to the wavelength distribution at Poker Flat which formed only single bell shape. This indicate that the LSTIDs at Mt. Moses is affected primarily by strong winds created by mountain waves associated to the region. Furthermore, the wave direction of propagation (shown in the polar plot in Figure 9) of both MSTIDs and LSTIDs over Poker Flat have predominantly southward component which is consist with the effect of prominent LSTIDs auroral source over the region. Moreover, the direction of wave propagation at Mt. Moses (shown in the polar plot in Figure 10) consist of two clear components: the southward and northward. This discrepancy can also be associated to the different source of AGW at Mt. Moses, middle latitude region. The AGW source at Mt. Moses is predominantly the mountain waves and strong winds compared to the AGW source at Poker Flat which result from persistent auroral energy associated to the region.

3.3 Limitations of the automated wave parameter computation approach

(1) The approach used to obtain the wave parameters is based on hourly data. This is done by iterating on each hour with two hours before and two hours after, which essentially sum-up to a 4 to 5-hour dataset which is equivalent to one satellite arc. This means that the signal processing is applied to each satellite pass for a single satellite to receiver pair. The limitation here is that hours at the edges are completed by day before (for 0 hour) and day after (for the 23rd hour). Sometimes these hours are not available for the either the day before or after and therefore the dataset is discarded. This contributed to why the distribution at the edges in Figure 9 and 10 is low compared to other hours.

(2) Since only 4 - 5-hour dataset is considered in our approach for the signal processing or filter analysis, the wave period above 2 hours may not be captured by our method. That is, a different of computing the wave parameter based on all 24 hours for each may show a slightly different result for the LSTIDs. This approach will be tested in future studies and in the part II of the research which is in progress.

4.0 Conclusion

In this study, we designed an automated algorithm that is capable of automatically detecting anomalous wave structures and computing basic wave parameters such as wave period, horizontal phase velocity, amplitude, wave propagation direction and wavelength. We analyzed three rocket lunch events of 2015 as showed in table 1 and compute different wave parameters to validate our approach. Our analyses demonstrate that the rocket lunch events trigger ionospheric perturbation with wave structures moving with 580 – 600 m/s in the southeastward direction. We also specify that lunch apogee could have significant impact on the time of wave arrival at the ionospheric altitudes (300km). The wave detection algorithm was also used to study the morphological and statistical distribution of LSTIDs and MSTIDs from 11 year of GNSS-TEC data over Poker Flat and Mt. Moses. This analysis reveals that MSTIDs over Poker Flat and Mt. Moses have similar occurrence morphology, however the morphology of LSTIDs over Poker Flat is very different from that of Mt. Moses, with Poker Flat exhibiting higher occurrence rate of LSTIDs compared to Mt. Moses. This is expected because Poker Flat is a location over high latitude where there are intermittent auroral energy inputs which are principal source of LSTIDs (see Jonah et al. 2018 and Zhang et al. 2019). The directions of propagation observed in this study are consistent with literatures. The automatic wave detection algorithm described in this paper can be applied to many areas, including: (1) apply to other GNSS TEC data from receivers anywhere around the world (2) easily apply in climatology study of wave analyses. (3) serves as input into innovative machine learning (ML) algorithms ABCGAN (e.g. Valentic 2023) designed to characterize background plasma parameters of the ionosphere and predict wave-like high/low-frequency perturbations during set of conditional drivers. The actual radar data and wave parameters from GNSS data and drivers used to train the ABCGAN has been published as ABCdata (e.g. Reyes et al. 2023). (4) serves as anomaly detection for real-time scenarios.

Reference

Afraimovich, E. L., Kosogorov, E. A., & Plotnikov, A. V. (2002). Shock-acoustic waves generated during rocket launches and earthquakes. Cosmic Research, 40(3), 241–254. https://doi.org/10.1023/A:1015925020387.

Alexander, M. J. (1996), A simulated spectrum of convectively generated gravity waves: Propagation from the tropopause to the mesopause and effects on the middle atmosphere, J. Geophys. Res., 101, 1571–1588, doi:10.1029/95JD02046.

Artru, J., V. Ducic, H. Kanamori, P. Lognonń e, and M. Murakami (2005), Ionospheric detection of gravity waves induced by tsunamis, Geophys. J. Int., 160, 840–848, doi:10.1111/j.1365-246X.2005.02552.x.

Azeem, I., Yue, J., Hoffmann, L., Miller, S. D., Straka, W. C., & Crowley, G. (2015). Multisensor profiling of a concentric gravity wave event propagating from the troposphere to the ionosphere. Geophysical Research Letters, 42, 7874–7880. https://doi.org/10.1002/2015GL065903

Azeem, I., S. L. Vadas, G. Crowley, and J. J. Makela (2017), Traveling ionospheric disturbances over the United States induced by gravity waves from the 2011 Tohoku tsunami and comparison with gravity wave dissipative theory, J. Geophys. Res. Space Physics, 122, 3430–3447, doi:10.1002/2016JA023659.

Belehaki, A., Tsagouri, I., Altadill, D., Blanch, E., Borries, C., Buresova, D., Chum, J., Galkin, I., Juan, J.M., Segarra, A., Timoté, C., Tziotziou, K., Verhulst, T.,Watermann, J., (2020). An overview of methodologies for real-time detection, characterization and tracking of Traveling Ionospheric Disturbances developed in the TechTIDE project. Journal of Space Weather and Space Climate 10. doi:10.1051/swsc/2020043

Blewitt G (1990) An automatic editing algorithm for GPS data. Geophys Res Lett 17(3):199–202

Borries, C., Ferreira, A.A. Nykiel, G. et al., A new index for statistical analyses and prediction of traveling ionospheric disturbances. Journal of Atmospheric and Solar–Terrestrial Physics (2023), doi: https://doi.org/10.1016/j.jastp.2023.106069

Bowling, T., Calais, E., & Haase, J. S. (2013). Detection and modeling of the ionospheric perturbation caused by a space shuttle launch using a network of ground-based Global Positioning System stations. Geophysical Journal International, 192(3), 1324–1331. https://doi.org/10.1093/gji/ggs101

Coster, A. J., Goncharenko, L., Zhang, S., Erickson, P. J., Rideout, W., & Vierinen, J. (2017). GNSS observations of ionospheric variations during the 21 August 2017 solar eclipse. Geophysical Research Letters, 44, 12,041–12,048. https://doi.org/10.1002/2017GL075774

Ding, F., Wan, W., Ning, B., & Wang, M. (2007). Large-scale traveling ionospheric disturbances observed by GPS total electron content during the magnetic storm of 29-30 October 2003. Journal of Geophysical Research, 112, A06309. https://doi.org/10.1029/2006JA012013

Drobzheva, Ya. M. Krasnov, V. V. Sokolova, O.I. (2003), Disturbances of the ionosphere of blast and acoustic waves generated at ionospheric heights by rockets, Journal of Atmospheric and Solar-Terrestrial Physics, https://doi.org/10.1016/j.jastp.2003.07.006

Chou, M.-Y., Lin, C. C. H., Shen, M.-H., Yue, J., Huba, J. D., & Chen, C.-H. (2018). Ionospheric disturbances triggered by SpaceX Falcon Heavy. Geophysical Research Letters, 45, 6334–6342. https://doi.org/10.1029/2018GL078088

Figueiredo, C. A. O. B., C. M. Wrasse, H. Takahashi, Y. Otsuka, K. Shiokawa, and D. Barros (2017), Large-scale traveling ionospheric disturbances observed by GPS dTEC maps over North and South America on Saint Patrick's Day storm in 2015, J. Geophys. Res. Space Physics, 122, 4755–4763, doi:10.1002/2016JA023417.

Fuller-Rowell, T. J., Codrescu, M. V., Mo-ett, R. J., & Quegan, S. (1996). On the seasonal response of the thermosphere and ionosphere to geomagnetic storms. Journal of Geophysical Research, 101, 2343–2353.

Habarulema, J. B., Yizengaw, E., Katamzi-Joseph, Z. T., Moldwin, M. B., & Buchert, S. (2018). Storm time global observations of large-scale TIDs from ground-based and in situ satellite measurements. Journal of Geophysical Research: Space Physics, 123, 711–1159 724. https://doi.org/10.1002/2017JA024510

Haralambous, H.; Paul, K.S. Travelling Ionospheric Disturbance Direction of Propagation Detection Using Swarm A-C In-Situ Electron Density. Remote Sens. 2023, 15, 897. https://doi.org/10.3390/rs15040897

Heale, C. J., Bossert, K., Vadas, S. L.,Hoffmann, L., Dörnbrack, A.,Stober, G., et al. (2020). Secondarygravity waves generated by breakingmountain waves over Europe.Journalof Geophysical Research: Atmospheres,125, e2019JD031662. https://doi.org/10.1029/2019JD031662

Hines, C. O. (1967), On the nature of travelling ionospheric disturbances launched by low-altitude nuclear explosions, J. Geophys. Res., 72, 1877–1882, doi:10.1029/JZ072i007p01877.

Hocke, K., & Schlegel, K. (1996). A review of atmospheric gravity waves and travelling ionospheric disturbances: 1982-1995. Annales Geophysicae, 14(9), 917–940. https://doi.org/10.1007/s00585-996-0917-6

Hocking, W.K. (2001), Buoyancy (gravity) waves in the atmosphere, https://physics.uwo.ca/~whocking/p103/grav_wav.html

Holton, J. R., and M. J. Alexander (1999), Gravity waves in the mesosphere generated by tropospheric convection, Tellus A-B, 51, 45–58, doi:10.3402/tellusb.v51i1.16259.

Horvath, I., & Lovell, B. C. (2010). Large-scale traveling ionospheric disturbances impacting equatorial ionization anomaly development in the local morning hours of the Halloween Superstorms on 29–30 October 2003. Journal of Geophysical Research, 115, A04302. https://doi.org/10.1029/2009JA014922

Hunsucker, R. D. (1982). Atmospheric gravity waves generated in the high-latitude ionosphere: A review. Reviews of Geophysics, 20(2), 293–315. https://doi.org/10.1029/RG020i002p00293

Jonah, O.F., Coster, A., Zhang, S., Goncharenko, L., Erickson, P.J., de Paula, E.R., & Kherani, E.A. (2018), TID Observations and Source Analysis During the 2017 Memorial Day Weekend Geomagnetic Storm over North America. *Journal of Geophysical Research: Space Physics*, 123. https://doi.org/10.1029/ 2018JA025367.

Jonah, O. F., Kherani, E. A., & de Paula, E. R. (2016). Observation of TEC perturbation associated with medium-scale traveling ionospheric disturbance and possible seeding mechanism of atmospheric gravity wave at a Brazilian sector. Journal of Geophysical Research: Space Physics, 121, 2531–2546. https://doi.org/10.1002/2015JA022273

Jonah, O. F., Kherani, E. A., & De Paula, E. R. (2017). Investigations of conjugate MSTIDS over the Brazilian sector during daytime. Journal of Geophysical Research: Space Physics, 122, 9576–9587. https://doi.org/10.1002/2017JA024365

Jonah, O. F., Zhang, S., Coster, A., Goncharenko, L., Erickson, P. J., Rideout, W., et al. (2020). Understanding the inter-hemispheric traveling ionospheric disturbances and their mechanisms. Remote Sensing, 12, 228. https://doi.org/10.3390/rs12020228

Jonah, O. F., Vergados, P., Krishnamoorthy, S., & Komjathy, A. (2021). Investigating ionospheric perturbations following the 2020 Beirut explosion event. Radio Science, 56, e2021RS007302. https://doi.org/10.1029/2021RS007302

Karlov, V. D., Kozlov, S. I., & Tkachev, G. N. (1980). Large-scale disturbances of the ionosphere occurring during the flight of a rocket with a working engine/Review. Kosmicheskie Issledovaniia, 18, 266-277.

Kherani, E. A., M. A. Abdu, E. R. de Paula, D. C. Fritts, J. H. A. Sobral, and F. C. de Meneses Jr. (2009), The impact of gravity waves rising from convection in the lower atmosphere on the generation and nonlinear evolution of equatorial bubble, Ann. Geophys., 27, 1657–1668, doi:10.5194/angeo-27-1657-2009.

Komjathy A, Sparks L, Wilson BD, Mannucci AJ (2005) Automated daily processing of more than 1,000 groundbased GPS receivers for studying intense ionospheric storms. Radio Sci 40, RS6006. DOI 10.1029/2005RS003279

Komjathy, A., Yang, Y.-M., Meng, X., Verkhoglyadova, O., Mannucci, A. J., & Langley, R. B. (2016). Review and perspectives: Understanding natural-hazards-generated ionospheric perturbations using GPS measurements and coupled modeling. Radio Science, 51, 951–961. https://doi.org/10.1002/2015RS005910

Kotake, N., Otsuka, Y., Tsugawa, T., Ogawa, T., & Saito, A. (2006). Climatological study of GPS total electron content variations caused by medium-scale traveling ionospheric disturbances. Journal of Geophysical Research, 111, A04306. https://doi.org/10.1029/2005JA011418

Lane, T. P., M. J. Reeder, and T. L. Clark (2001), Numerical modeling of gravity wave generation by deep tropical convection, J. Atmos. Sci., 58, 1249–1274, doi:10.1175/1520-0469(2001)058<1249:NMOGWG>2.0.CO;2.

Lastovicka, J., Akmaev, R. A., Beig, G., Bremer, J., & Emmert, J. T. (2006). Global change in the upper atmosphere. Science, 314(5803), 1253– 1254. https://doi.org/10.1126/science.1135134

Lin, C. H., Chen, C.-H., Matsumura, M., Lin, J.-T., & Kakinami, Y. (2017b). Observation and simulation of the ionosphere disturbance waves triggered by rocket exhausts. Journal of Geophysical Research: Space Physics, 122, 8868–8882. https://doi.org/10.1002/2017JA023951.

Lin, C. H., Shen, M.-H., Chou, M.-Y., Chen, C.-H., Yue, J., Chen, P.-C., & Matsumura, M. (2017a). Concentric traveling ionospheric disturbances triggered by the launch of a SpaceX Falcon 9 rocket. Geophysical Research Letters, 44, 7578–7586. https://doi.org/10.1002/2017GL074192.

Liu, J. Y., Y. B. Tsai, K. F. Ma, Y. I. Chen, H. F. Tsai, C. H. Lin, M. Kamogawa, and C. P. Lee (2006), Ionospheric GPS total electron content (TEC) disturbances triggered by the 26 December 2004 Indian Ocean tsunami, J. Geophys. Res., 111, A05303, doi:10.1029/2005JA011200.

Lognonńe, P., J. Artru, R. Garcia, F. Crespon, V. Ducic, E. Jeansou, G. Occhipinti, J. Helbert, G. Moreaux, and P. Godet (2006), Ground-based GPS imaging of ionospheric postseismic signal, Planet. Space Sci., 54, 528–540, doi:10.1016/j.pss.2005.10.021.

Mannucci AJ, Wilson BD, Yuan DN, Ho CH, Lindqwister UJ, Runge TF (1998) A global mapping technique for GPSderived ionospheric total electron content measurements. Radio Sci 33(3):565–583

McLandress, C., Shepherd, T. G., Polavarapu, S., & Beagley, S. R. (2012). Is missing orographic gravity wave drag near 60°S the cause of the stratospheric zonal wind biases in chemistry—Climate models? Journal of the Atmospheric Sciences, 69(3), 802– 818. https://doi.org/10.1175/JAS-D-11-0159.1

Meng, X., Vergados, P., Komjathy, A., & Verkhoglyadova, O. (2019). Upper atmospheric responses to surface disturbances: An observational perspective. Radio Science, 54. https://doi.org/10.1029/2019rs006858

Mendillo, M. (1981). The effect of rocket launches on the ionosphere. Advances in space research, 1(2), 275-290.

Nishioka, M., T. Tsugawa, M. Kubota, and M. Ishii (2013), Concentric waves and short-period oscillations observed in the ionosphere after the 2013 Moore EF5 tornado, Geophys. Res. Lett., 40, 5581–5586, doi:10.1002/2013GL057963.

Reyes, Pablo, Lamarche, Leslie, & Jonah, Olusegun. (2023). ABCdata (2.0) [Data set]. Zenodo. https://doi.org/10.5281/zenodo.8062282

Richmond, A. D. (1978). Gravity wave generation, propagation, and dissipation in the thermosphere. Journal of Geophysical Research, 83, 4131– 4145. https://doi.org/10.1029/JA083iA09p04131

Rolland, L. M., G. Occhipinti, P. Lognonné, and A. Loevenbruck (2010), Ionospheric gravity waves detected offshore Hawaii after tsunamis,Geophys. Res. Lett., 37, L17101, doi:10.1029/2010GL044479.

Savastano, G. (2018). New applications and challenges of GNSS variometric approach (Doctoral dissertation). The University of Rome "LaSapienza". Retrieved from http://hdl.handle.net/11573/1077041

Savitzky, A., & Golay, M. J. E. (1964). Smoothing and differentiation of data by simplified least squares procedures. Analytical Chemistry, 36, 1627–1639.

Snively, J. B., and V. P. Pasko, Breaking of thunderstorm-generated gravity waves as a source of short-period ducted waves at mesopause altitudes, Geophys. Res. Lett., 30(24), 2254, doi:10.1029/2003GL018436, 2003.

Tsugawa, T., A., Saito, Y. Otsuka, and M., Yamamoto (2003) Damping of large-scale traveling ionospheric disturbances detected with GPS networks during the geomagnetic storm, Journal of Geophysical Research, vol. 108, no. A3, 1127, doi:10.1029/2002JA009433.

Tsugawa, T., Saito, A., & Otsuka, Y. (2004). A statistical study of large-scale traveling ionospheric disturbances using the GPS network in Japan. Journal of Geophysical Research, 109, 669. https://doi.org/10.1029/2003JA010302

Vadas, S. L. (2007), Horizontal and vertical propagation and dissipation of gravity waves in the thermosphere from lower atmospheric and thermospheric sources, J. Geophys. Res., 112, A06305, doi:10.1029/2006JA011845.

Vadas, S. L., and D. C. Fritts (2009), Reconstruction of the gravity wave field from convective plumes via ray tracing, Ann. Geophys., 27, 147–177, doi:10.5194/angeo-27-147-2009.

Vadas, S. L., and G. Crowley (2010), Sources of the traveling ionospheric disturbances observed by the ionospheric TIDDBIT sounder near Wallops Island on 30 October 2007, J. Geophys. Res., 115, A07324, doi:10.1029/2009JA015053

Vadas, S. L., H.-L. Liu, and R. S. Lieberman (2014), Numerical modeling of the global changes to the thermosphere and ionosphere from the dissipation of gravity waves from deep convection, J. Geophys. Res. Space Physics, 119, 7762–7793, doi:10.1002/2014JA020280.

Vadas, S. L., J. Yue, and T. Nakamura (2012), Mesospheric concentric gravity waves generated by multiple convection storms over the North America Great Plain, J. Geophys. Res., 117, D07113, doi:10.1029/2011JD017025.

Valentic, Todd. (2023). ABCGAN (v3.0.0). Zenodo. https://doi.org/10.5281/zenodo.7747377

Vierinen, J., A. J. Coster, W. C. Rideout, P. J. Erickson, and J. Norberg (2016) Statistical framework for estimating GNSS bias, Atmos. Meas. Tech., 9, 1303–1312, https://doi.org/10.5194/amt-9-1303-2016.

Zakharenkova, I., E. Astafyeva, andI. Cherniak (2016), GPS and GLONASSobservations of large-scale travelingionospheric disturbances during the2015 St. Patrick's Day storm, J. Geophys.Res. Space Physics,121, 12,138–12,156,doi:10.1002/2016JA023332

Zhang, S.-R., Erickson, P. J., Coster, A. J., Rideout, W., Vierinen, J., Jonah, O. F., & Goncharenko, L. P. (2019). Subauroral and polar traveling ionospheric disturbances during the 7–9 September 2017 storms. Space Weather, 17, 1748–1764. https://doi.org/10.1029/2019SW002325

Zhang, S., Erickson, P. J., Goncharenko, L., Coster, A. J., Rideout, W., & Vierinen, J. (2017). Ionospheric bow waves and perturbations induced by the 21 august 2017 solar eclipse. Geophysical Research Letters, 44, 12,067–12,073. https://doi.org/10.1002/2017GL076054

Acknowledgement

This material is based on work supported by the Defense Advanced Research Projects Agency (DARPA) under Contract No. HR001121C0026.
Special thanks to MIT Haystack and Bill Rideout for providing the access to TEC processing resources and Madrigal database which facilitate the TEC data processing in this study.